Scientific Research Publishing

Journal of Water Resource and Protection, 2025, 17(9), 678-695
https://www.scirp.org/journal/jwarp
ISSN Online: 1945-3108
ISSN Print: 1945-3094

Oil Spill-Related Coastal Pollution in Madingo-Kayes, Republic of Congo

Jean Bienvenu Dinga[1,2*], Christ Mokomba Madzo Makouezi[1,2], Auguste Merveilles Bawatokobuta Nanitelamio[1], Wilfrid Innocent Ndebeka[1]

[1]Faculté des Sciences et Techniques, Université Marien Ngouabi, Brazzaville, The Republic of Congo
[2]Institut National de Recherches en Sciences Exactes et Naturelles (IRSEN), Cité Scientifique (Ex-ORSTOM), Brazzaville, The Republic of Congo
Email: *bvs_dinga@yahoo.fr

How to cite this paper: Dinga, J.B., Makouezi, C.M.M., Nanitelamio, A.M.B. and Ndebeka, W.I. (2025) Oil Spill-Related Coastal Pollution in Madingo-Kayes, Republic of Congo. *Journal of Water Resource and Protection*, **17**, 678-695.
https://doi.org/10.4236/jwarp.2025.179036

Received: May 9, 2025
Accepted: September 21, 2025
Published: September 24, 2025

Abstract

The environmental impacts caused by frequent oil spills along the Congolese coast pose a significant concern. The main objective of this work is to study the dynamics of coastal pollution due to hydrocarbons using hyperspectral images in the Madingo-Kayes area, located in the Kouilou department in the southwest of the Republic of Congo. To achieve this, two multi-temporal Hyperion hyperspectral datasets, acquired by the EO-1 satellite on February 18, 2014, and December 30, 2016, respectively, were retrieved from the USGS database. These images were then analyzed and processed using ENVI 5.0 and QGIS 3.16 software to detect and map surface hydrocarbon indicators in the study area using three methods. The first method is based on the calculation of sub-band ratios in the absorption wavelength ranges of hydrocarbons (1700 - 1800 and 2300 - 2350 nm). The HD ratio detected 443 hydrocarbon indicators in the 2014 Hyperion image, while 629 indicators were detected in the 2016 image. The HI ratio detected 155 indicators in 2014, compared to 133 in 2016. The second method is the SAM classification, based on prototype hydrocarbon absorption signatures. It detected 387 indicators in the 2014 image and 73 in the 2016 image. The third method is the SSM classification, based on vegetation stress signatures caused by hydrocarbons within the 680–740 nm wavelength range. It detected 168 hydrocarbon-related indicators in vegetation in 2014 and 18 in 2016.

Keywords

Dynamics, Coastal Pollution, Hydrocarbons, Hyperspectral Images, Kouilou

1. Introduction

The Republic of Congo, one of Africa's leading crude oil producers [1], has a

coastline that is subject to intense oil activity. The country's economy is essentially based on oil, which accounts for around 90% of exports [1] [2], two-thirds of national GDP, and 80% of government revenue [3]. The country's territorial waters are home to oil infrastructures that pose a permanent and real threat of pollution [4]. Pollution also comes from neighbouring countries, carried by sea currents [5] and wind [6]. Oil slicks have been observed on the coast of Gabon [7] and in the Gulf of Guinea [8].

Assessing the extent of the evolution of this pollution remains a challenge. Numerous studies have highlighted the environmental impact of oil spills on the Congolese coast [2] [5] [9]-[11]. The environmental consequences are dramatic: degradation of soil and water, contamination and mortality of fish, damage to fishing gear and boats, damage to commercial fishing, negative impacts on tourism, incidence of diseases such as digestive, cardiac and neurological disorders, lung disease, skin rashes, mucous membrane disorders, and breathing difficulties.

This study focuses specifically on the Madingo-Kayes area because of several factors that make it a site of interest for coastal pollution research. Firstly, the area is an oil exploration and production site [1]. The presence of oil infrastructure increases the risk of oil spills, making it a relevant site for studying environmental impacts. For example, an oil spill occurred on 20 January 2011 in the Madingo-Kayes district, at one of Sintoukola Potash's potash exploration sites, causing major damage in the villages of Sintoukola and Nkoutou. Around 600 people were evacuated from the surrounding villages. In addition, the Madingo-Kayes coastal zone is home to sensitive ecosystems, such as mangroves and marshy areas, which are particularly vulnerable to oil pollution. Organisms living in the mangrove ecosystem can suffer both the direct effects of oil and, in the longer term, the loss of their habitat [12]. The study of pollution in this area also makes it possible to assess the socio-economic consequences of oil spills for the local population, which depends on natural resources for its livelihood, including small-scale inland fishing [13]. Tourism can be destabilised by the presence of oil slicks in the water and tar balls on the coast.

Nowadays, remote sensing, and more specifically hyperspectral imagery, is widely used for exploring and monitoring oil pollution [6] [14]-[19]. Hyperspectral images can be used to identify hydrocarbons using absorption between 1700 - 1800 nm and 2300 - 2350 nm [20] [21], with peaks at 1730 nm and 2310 nm [20] [22]-[24]. These specific absorption bands highlight the presence of hydrocarbons mixed with sand [20] [25]. Several methods have been developed to detect hydrocarbon indicators: the calculation of sub-band ratios such as Hydrocarbon Detection (HD) [26] and Hydrocarbon Index (HI) [27], the use of spectral signatures in the absorption bands at 1700 nm and 2300 nm [25] [28], and 680 - 740 nm for hydrocarbon-contaminated vegetation [29]-[31].

The aim of this work is to study the dynamics of coastal oil pollution using hyperspectral images in the Madingo-Kayes area, with a view to analysing the spatio-temporal dynamics of oil pollution and setting up a remote pollution monitoring tool to supplement existing data and increase observation capacity along

the Congolese coast. The study will thus contribute to a better understanding and management of this major environmental problem.

2. Presentation of the Study Area

2.1. Physical Environment

The study area is located in Madingo-Kayes, in the department of Kouilou, in the south-west of the Republic of Congo, between latitudes 4˚22'6.25" and 4˚25'58.34" south and between longitudes 11˚34'22.28" and 11˚40'58.29" east (**Figure 1**). It covers an area of around 55 km^2. The area is bounded to the north by lakes Louandjili and Ndembo, to the south and west by the Atlantic Ocean, to the north-west by the village of Bellelo, and to the east by the Route Nationale 5 (Madingo-Kayes-Nzambi). Madingo-Kayes is a district located around 42 km from Pointe-Noire, the country's economic capital, and is home to the largest deep-water port in Central Africa. The climate is humid tropical [32] [33], with alternating hot rainy seasons (October-May) and cool dry seasons (June-September) [32]-[34]. Average annual rainfall is around 1282 mm [33]. The topography comprises three main elements: plateaux, large valleys, and a coastal plain. Altitude is generally less than 150 m [34]. Vegetation is dominated by a forest-savannah mosaic [32] [34]-[37]. The hydrographic network is organised around two types of water-course [32] [34]: small rivers originating on the western edge of the coastal plateau and the Kouilou River. Its average flow is 913 m^3/s at Sounda and 1150 m^3/s at its mouth. The soil types encountered in the study area are [38] [39]: poorly developed soils, hydromorphic soils, podzolic soils, and highly desaturated ferralitic soils, which are by far the most widespread. All the soils derive from loose original materials, which are the sands of the Cirques series [38] [39], of Miocene to Pliocene age, forming a fluvial to deltaic glacis that covers the entire coastal basin and overlies the Mesozoic substratum in unconformity [40].

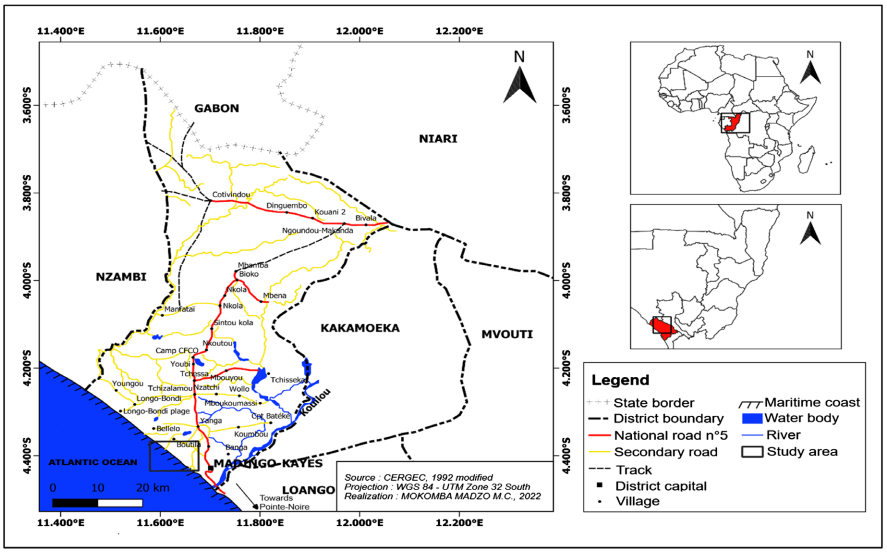

Figure 1. Geographical location and map of the study area (CERGEC, 1992 modified).

2.2. Wind Regime

2.2.1. Wind Direction

Winds blow most often from the west (August-October) and from the south (October-August). The prevailing moderate to strong winds (2 to 5 m/s) are from the south and south-west, decreasing in frequency from south (50.0%) to south-west (16.7%). The south-westerly wind blows continuously throughout the year [33]. Moderate easterly winds (2 to 3 m/s) are less frequent and blow from east to west. Northerly winds are fairly rare.

2.2.2. Types of Wind

There are calm winds (67.7% of observations), with an average speed of less than 1.0 m/s, and non-calm winds, with an average speed of 1.5 m/s.

In addition to the general winds, there are local winds (land and sea breezes) perpendicular to the coast at any time of the year [33].

2.3. Oceanic Factors

2.3.1. Tides

The tidal range is relatively small (0.60 m to 1.70 m) [41].

2.3.2. Currents

1) Tidal currents

Tidal currents generally run parallel to the coast [42].

2) General ocean currents

Several general ocean currents influence the area, including the South Equatorial Current, the South Equatorial Counter Current, the trade wind drift, the Angola Current, and the Benguela Current [43].

2.3.3. Swells

Swells have long periods (10 s to 15 s) and significant heights (3 m and 4.5 m), with a south to south-westerly direction [41]. The south-west to north-east swell is present all year round, with maximum intensity during the dry season [34].

2.3.4. Water Temperature

Sea surface temperatures vary between 25 and 30˚C [43].

3. Materials and Methods

3.1. Materials

This study required the use of Hyperion multitemporal hyperspectral image data acquired on 18 February 2014 at 08:28:49 and 30 December 2016 at 06:49:55, respectively, during NASA's New Millennium Program EO-1 space mission [44], and archived in the USGS database [45]. The downloaded hyperspectral image data are in the form of L1R (HDF format) and L1Gst (Geotiff format) products. They were processed using two software packages: ENVI 5.0 and QGIS 3.16. **Table 1** shows the specifications of the Hyperion EO-1 sensor.

Table 1. Specifications of the EO-1 hyperion sensor.

Number of Bands	Spectral Range (nm)	Spectral Resolution (nm)	Spatial Resolution (m)	Radiometric Resolution (bit)	Temporal Resolution (days)
242	400 - 2500	10	30	16	16

3.2. Methodology

3.2.1. Image Pre-Processing

The images were pre-processed using ENVI 5.0 software, which involved first reducing the images over the study area (to approximately 55 km^2) to 'standard ENVI' format. After this operation, 46 bad bands (1 - 7, 58 - 76, and 225 - 242) were eliminated, leaving only 198 good bands (8 - 57 and 77 - 224). The bands, which are generally due to imperfect calibration, were then removed from the images. Taking into account sensor irregularities, sensor noise, and atmospheric noise, the 198 good bands were calibrated, and the data in ".BSQ" format were converted to ".BIL" format so that they could accurately represent the reflected or emitted radiation measured (reflectance) by the sensor. Next, the atmospheric correction of the FLAASH universal model was applied to the images to reduce the effects of the atmosphere (vapor, dust, gases, aerosols, etc.) emitted at the Earth's surface and to obtain the reflectance of the surface; the scaling factor is 400 for the VNIR channels (bands 8 - 57) and 800 for the SWIR channels (bands 77 - 224). After atmospheric correction, the water vapor absorption bands were removed (121 - 130 and 166 - 180 for the 2014 Hyperion image; 120 - 133 and 165 - 181 for the 2016 Hyperion image), then applied band by band, under Band Math, to correct for negative reflectance values and spectral aberrations, using the Post FLAASH equation:

$$(b1\ le\ 0)0+(b1\ ge\ 10000)1+(b1\ gt\ 0 \text{ and } b1\ lt\ 10000)*float(b1)/10000 \quad (1)$$

where, *b*: band, *le*: less than or equal to, *lt*: less than, *ge*: greater than or equal to, *gt*: greater than.

Finally, geometric correction was carried out on the basis of ground control points (GCP), using the L1 Gst image as a reference image in order to assign the actual ground coordinates to the L1 R image. The images were then reprojected onto the WGS84-UTM projection system, Zone 32S.

3.2.2. Image Processing

Image processing began with ENVI 5.0 and was completed with QGIS 3.16. It consisted of detecting and mapping hydrocarbon indications on the surface of the study area using three methods. The first method is based on the calculation of sub-band ratio indices using the HD (Hydrocarbon Detection) and HI (Hydrocarbon Index) algorithms over the hydrocarbon absorption wavelength intervals (1700 - 1800 and 2300 - 2350 nm).

The hydrocarbon detection ratio (HD) was calculated using the formula in [26]:

$$\mathrm{HD} = \frac{B_A + B_C}{2 * B_B} \quad (2)$$

If HD ≥ 1, hydrocarbon indices are detected; B_A, B_B and B_C represent the absorption bands of surface objects.

The hydrocarbon index (HI) was calculated using the formula in [27]:

$$HI = \frac{2}{3}\left(R_C - R_A\right) + R_A - R_B \quad (3)$$

If HI ≳ 0, the surfaces are affected or contaminated by hydrocarbons; R_A, R_B and R_C are the spectral reflectance values of the surface objects.

The second method is the SAM (Spectral Angle Mapper) classification, based on the prototypical signatures (endmembers) of hydrocarbon absorption, extracted from the images after unmixing or demixing (one-by-one spectral analysis) over the hydrocarbon absorption wavelength ranges (1700 - 1800 and 2300 - 2350 nm). The last method is the SSM (Spectral Similarity Mapper) classification, based on the signatures of vegetation stress by hydrocarbons over the 680 - 740 nm wavelength range. After the various classifications, the confusion matrices were applied to the reference images.

3.2.3. Hydrocarbon Index Mapping

To carry out this step, all the images obtained after processing in ENVI 5.0 were imported into QGIS 3.16 software in order to vectorize the hydrocarbon indices and produce hydrocarbon index maps.

3.2.4. Analysis of Oil Pollution Dynamics

The analysis of the spatio-temporal dynamics of hydrocarbon pollution consists of comparing the different hydrocarbon index maps in order to monitor the evolution of pollution in space and time, while determining the agents and dynamic factors driving the movements of this pollution in the environment between the years 2014 and 2016.

The adapted methodological approach is summarized in the figure below (**Figure 2**).

4. Results

4.1. Results Obtained from the Calculation of Index Sub-Band Ratios

4.1.1. Results of the Calculation of Indices Using the Hydrocarbon Detection (HD) Algorithm

The maps (**Figure 3**) are the results of applying the HD algorithm to Hyperion images. On the 2014 Hyperion image, the algorithm produced 443 hydrocarbon indices, including 167 in the 1700 to 1800 nm wavelength range and 276 in the 2300 to 2350 nm wavelength range. In contrast, on the 2016 Hyperion image, the algorithm produced 629 indices, including 177 in the 1700 to 1800 nm wavelength range and 452 in the 2300 to 2350 nm wavelength range. The indices are represented by several grayscale dots. Black and dark gray dots indicate strong indices, medium gray dots indicate medium indices, and light gray dots indicate weak indices.

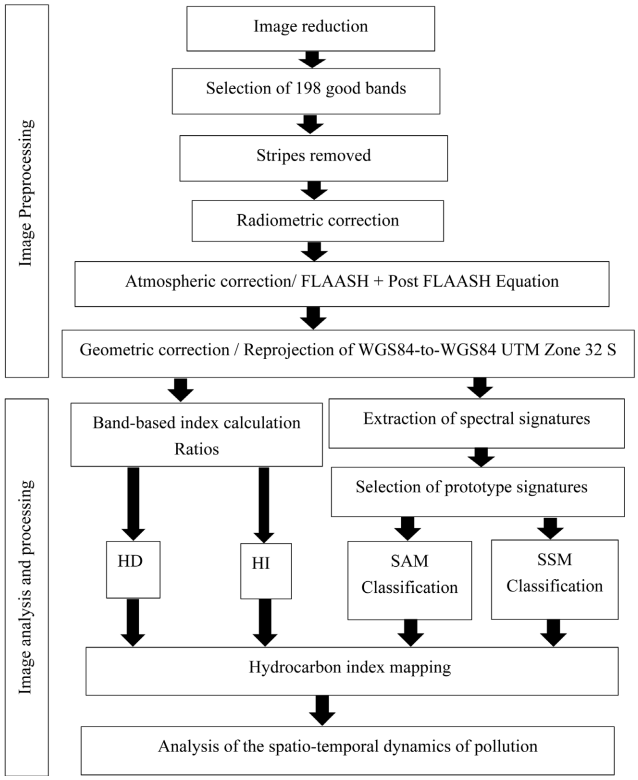

Figure 2. Adapted methodology.

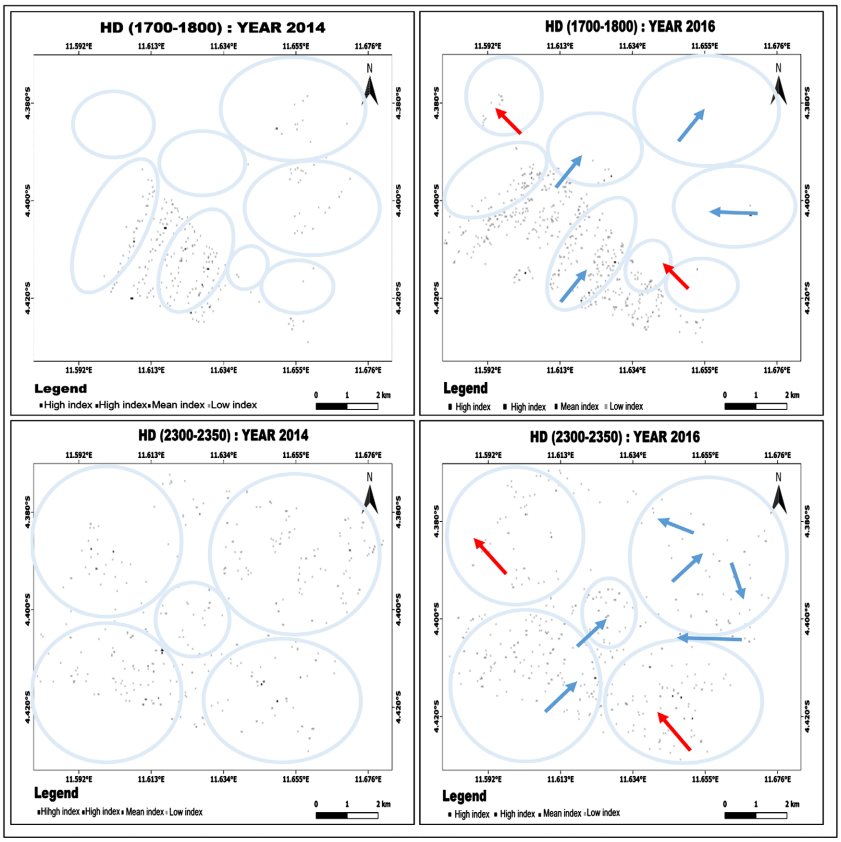

Figure 3. Result of the HD index calculation.

4.1.2. Results of Index Calculation Using the Hydrocarbon Index (HI) Algorithm

The maps (Figure 4) are the result of applying the HI algorithm to Hyperion images. On the 2014 Hyperion image, the algorithm produced 155 hydrocarbon indices (red dots), including 69 in the wavelength range from 1700 to 1800 nm and 86 in the wavelength range from 2300 to 2350 nm. In contrast, on the 2016 Hyperion image, the algorithm produced 133 hydrocarbon indices (red dots), including 70 in the wavelength range 1700 to 1800 nm and 63 in the wavelength range 2300 to 2350 nm.

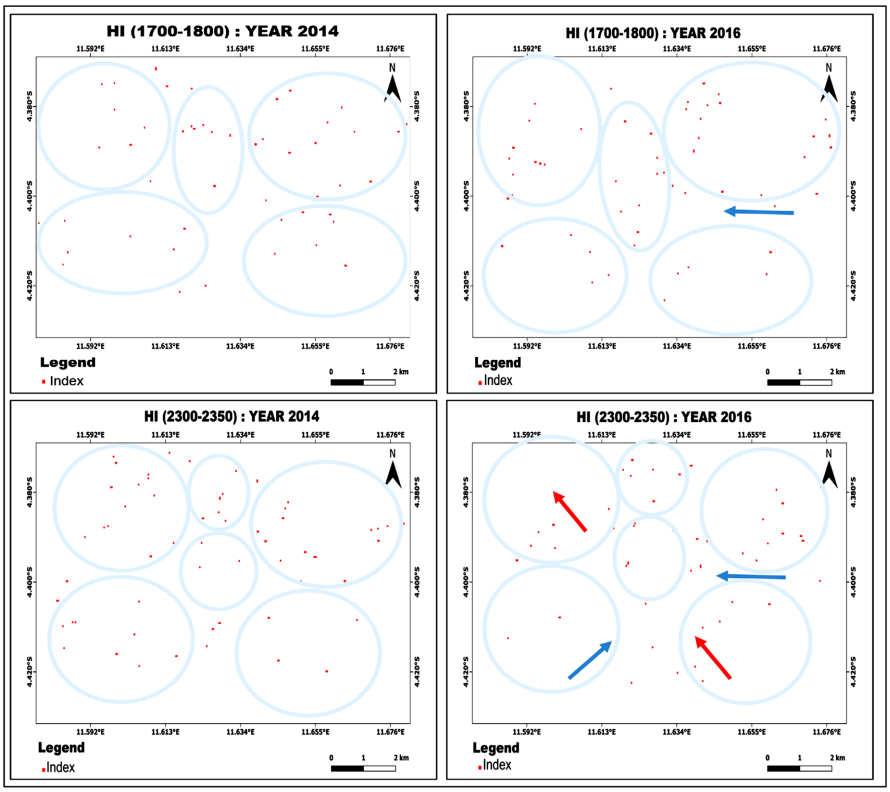

Figure 4. Result of the HI index calculation.

4.1.3. SAM (Spectral Angle Mapper) Classification Results

The maps (Figure 5) are the result of SAM classification, based on endmembers or prototypical absorption signatures of hydrocarbons. On the 2014 Hyperion image, the classification yielded 387 hydrocarbon endmembers (red dots), including 193 in the wavelength range 1700 to 1800 nm and 194 in the wavelength range 2300 to 2350 nm. In contrast, on the 2016 Hyperion image, the classification yielded 73 hydrocarbon indices (red dots), including 34 in the wavelength range 1700 to 1800 nm and 39 in the wavelength range 2300 to 2350 nm. The results are very similar to those obtained with SAM classification and the HD report on the 2300 to 2350 nm wavelength range. To evaluate the accuracy of the different classifications, confusion matrices were generated, including the overall accuracy, which was 100%, and the corresponding Kappa coefficient, which was 1.

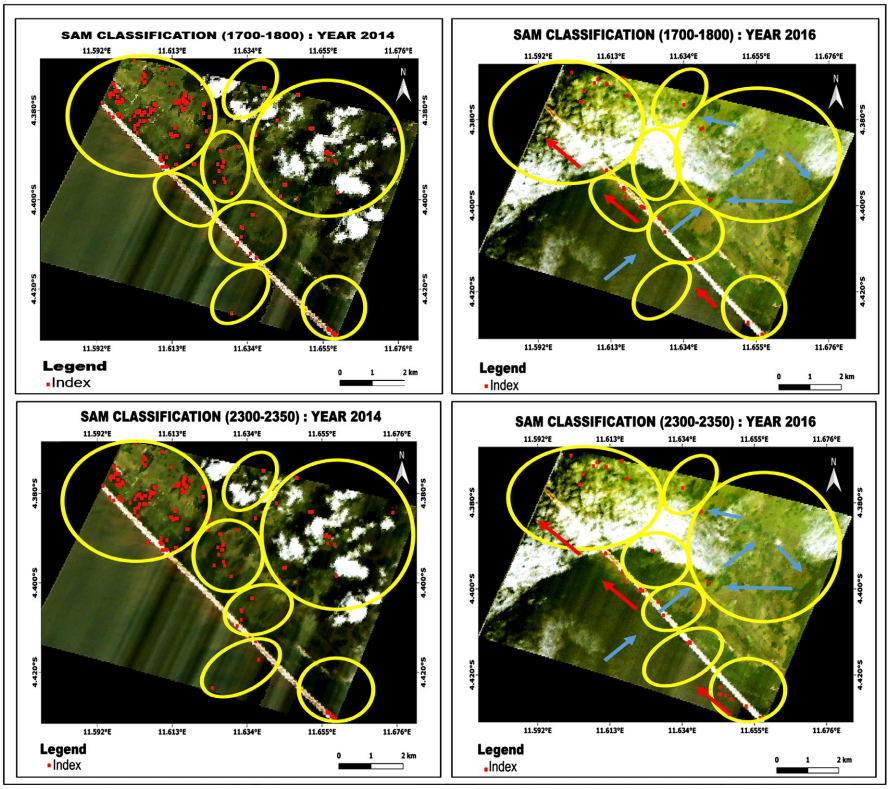

Figure 5. Hydrocarbon index results according to SAM classification.

4.1.4. Results of the SSM (Spectral Similarity Mapper) Classification

The maps (Figure 6) are the result of the SSM classification. The classification identified the presence of vegetation stress (green dots) linked to hydrocarbon contamination in the wavelength range from 680 to 740 nm. In the 2014 Hyperion image, 168 hydrocarbon indices were detected in the vegetation, while in the 2016 Hyperion image, 18 hydrocarbon indices were detected in the vegetation. The results are very similar to those obtained with SAM classification and the HD ratio. The confusion matrices for SSM classification gave an overall accuracy of 100% and a Kappa coefficient of 1.

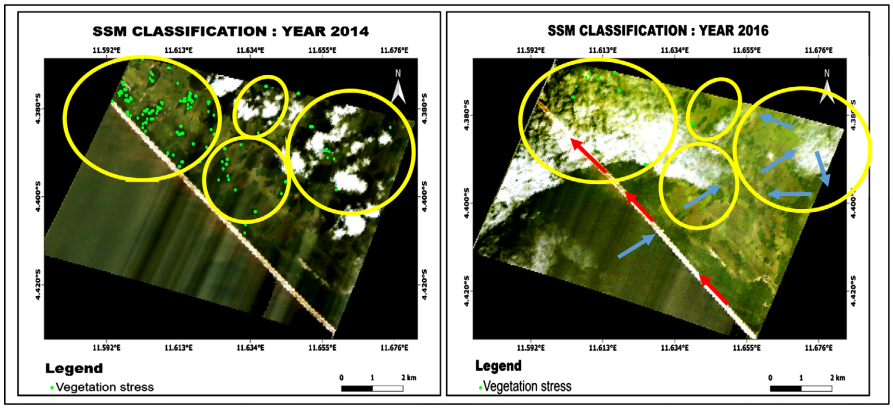

Figure 6. Result of vegetation stress according to the SSM classification in the wavelength range of 680 to 740 nm.

The table below summarizes the number of hydrocarbon indices obtained with the different methods used (Table 2).

Table 2. Summary of the results obtained.

Method	Number of Hydrocarbon Indices					
	Year 2014			Year 2016		
	680 - 740 nm	1700 - 1800 nm	2300 - 2350 nm	680 - 740 nm	1700 - 1800 nm	2300 - 2350 nm
HD		167	276		177	452
HI		69	86		70	63
SAM		193	194		34	39
SSM	168			18		

To illustrate the dynamics of hydrocarbon pollution in the study area as a function of ocean circulation, the following maps were developed (Figure 7).

5. Interpretation and Discussion

5.1. Analysis and Interpretation of the Spatio-Temporal Dynamics of Oil Pollution

5.1.1. Analysis Using the HD Algorithm

The maps obtained using the HD algorithm reveal a wide variety of hydrocarbon indices, ranging from white to black, corresponding to low to very high concentrations. In 2014, 443 indices were detected, compared to 629 in 2016, indicating a significant increase in the detection of hydrocarbons over this period. The relative stability of indices in the 1700-1800 nm wavelength range (167 in 2014 compared to 177 in 2016) contrasts with a notable increase in the 2300-2350 nm range (276 in 2014 compared to 452 in 2016).

Hydrocarbon indices are mainly located along the south-western sector, slightly in the south-eastern sector with a small migration towards the north-western sector, along the coast. Inland, the indices are located in the northeast and east sectors. In 2016, this trend became more pronounced, with increased concentration along these sectors, but a reduction inland, where they became almost invisible in some sectors.

5.1.2. Analysis with the HI algorithm

The maps obtained using the HI algorithm show a reverse trend: in 2014, 155 indices were detected, but this number decreased to 133 in 2016. This could indicate a reduction in the detection or presence of hydrocarbon indices according to this algorithm, despite the increase observed with HD. The distribution of indices remains relatively stable in both periods, but with a slight decrease in the 2300-2350 nm range.

Hydrocarbon indices are located in several areas, including offshore, along the coast, and inland.

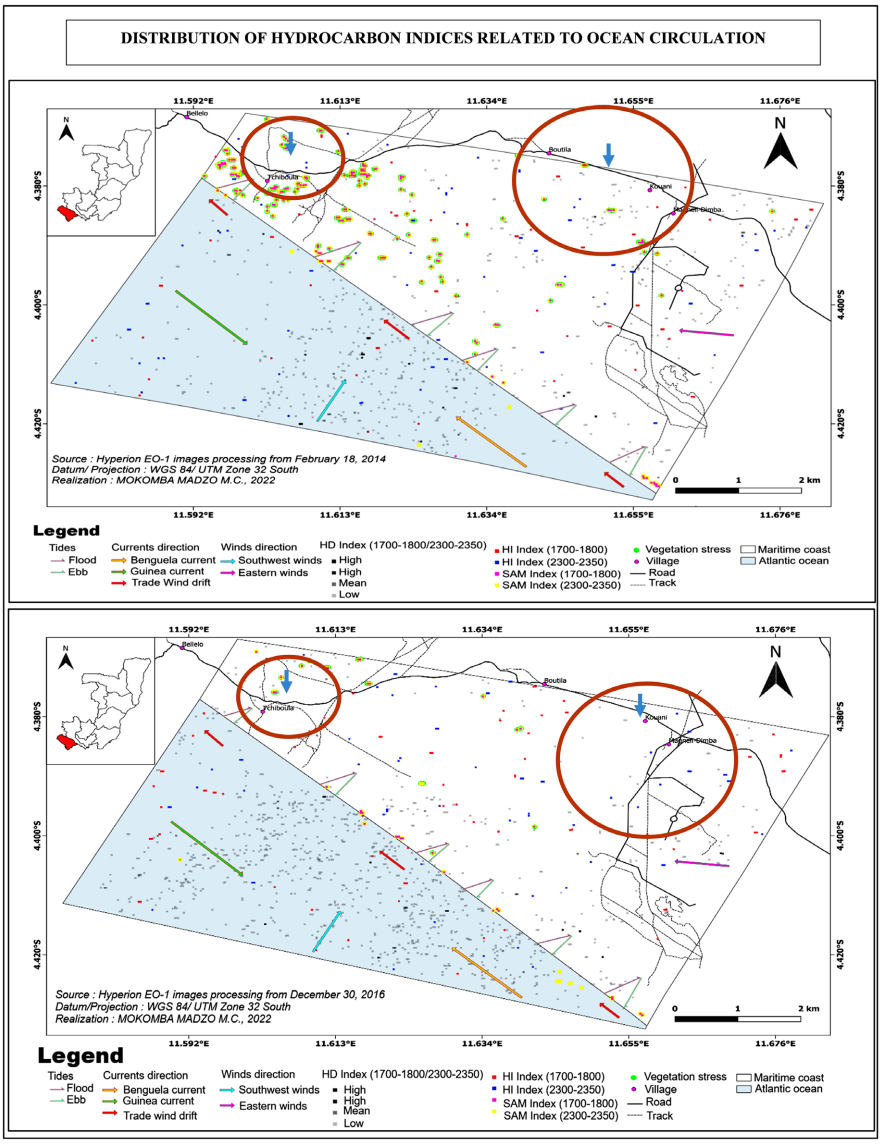

Figure 7. Distribution of hydrocarbon indices related to ocean circulation.

Ocean dynamics, influenced by winds and currents, particularly those of the trade winds, Benguela, and Guinea, explain the dispersion and migration of oil slicks. Surface currents, combined with natural degradation and coastal erosion, contribute to the displacement of hydrocarbons, creating a variable distribution along the coast and in the maritime zone.

5.1.3. Analysis Using SAM Classification

The SAM method, based on the absorption signature of hydrocarbons, shows a sharp reduction in the number of indices detected, from 387 in 2014 to only 73 in 2016. This significant decrease suggests a reduction in hydrocarbon pollution in the area. The spatial distribution indicates that, in 2014, hydrocarbons were present in several areas, particularly offshore and in certain inland locations, with high concentrations in the northwest. In 2016, this presence was significantly re-

duced, especially in land areas, indicating an improvement in environmental quality. The accuracy of this classification is excellent, with a success rate of 100% and a Kappa coefficient of 1, attesting to the reliability of the results.

5.1.4. Analysis Using the SSM Classification

This method, which indirectly detects hydrocarbon pollution via plant stress, confirms the downward trend. The reduction in the number of hydrocarbon indices in vegetation, from 168 in 2014 to 18 in 2016, indicates an improvement in plant health, probably linked to the decrease in pollution. The spatial distribution shows that, as with SAM, the presence of hydrocarbons was more pronounced in 2014, particularly in terrestrial and coastal areas, but decreased in 2016. The consistency between these two methods reinforces the credibility of the results.

5.1.5. Environmental and Dynamic Factors

Variations in the distribution and quantity of hydrocarbons can be explained by several factors. Dispersion at sea is influenced by wind dynamics, particularly south to south-westerly winds, reinforced by sea breezes, which spread and move oil slicks in the form of thin parallel bands. The deviation to the northeast and west is linked to ocean currents, such as the trade winds, Benguela and Guinea currents, as well as tidal currents. The fragmentation and burial of slicks by coastal erosion, combined with natural biodegradation, also explain the gradual reduction of hydrocarbons in certain areas.

On land, the reduction of hydrocarbons is due to several processes: dispersion, dissolution, evaporation, infiltration into the soil, formation of soluble or persistent products (tar balls), and biodegradation. Temperature, oxygen availability, and nutrients also play a role in hydrocarbon degradation. These processes explain the decrease in plant stress and the reduction in hydrocarbon indices detected in terrestrial areas.

5.1.6. Impact of Human Activities and Temporal Evolution

Analysis of the maps shows that oil pollution has decreased in several areas, particularly in the villages of Tchiboula, Kouani, and Magneli Dimba, located in the north-west and north-east (**Figure 7**). This decrease is probably linked to clean-up operations and a reduction in oil production. Production did indeed decline between 2014 (approximately 91.4 million barrels [46]) and 2016 (approximately 84.6 million barrels [47]), which could explain the decrease in spills and pollution.

5.2. Discussion

The main objective is to understand how pollution evolves in space and time by identifying the geographical distribution of hydrocarbons. The methodology is based on the use of hyperspectral images, which offer a valuable capability for remote monitoring of this pollution. The algorithms applied make it possible to detect hydrocarbon indices, thus confirming the presence of hydrocarbon pollution on the Congolese coast, in line with previous work [6].

The results obtained with the HD algorithm show an abundance of hydrocarbon indices, with a wide geographical distribution. However, there are differences compared to a previous study carried out with a Hyperion image in 2015 [6]. In particular, this study found more indices in the south-western sector at Madingo-Kayes, whereas the previous study did not detect as many in the Djéno terminal sector. The difference could be explained by the absence of MNF (Maximum Noise Fraction) processing in our study, which eliminates noise and improves detection.

Detection is more effective in the 2300 - 2350 nm range than in the 1700-1800 nm range, which contrasts with previous results [6]. The quality of the results may also be influenced by oceanographic and climatic factors, such as temperature, wind speed, and ocean circulation, which affect the degradation of hydrocarbons.

Unlike the previous study [6], where the presence of hydrocarbons was confirmed by laboratory analyses, here the indices detected by the HD algorithm have not yet been verified in the field. However, laboratory analyses in other Congolese sectors have confirmed the pollution [6] [9], highlighting the need to do the same in Madingo-Kayes.

The results obtained with the HI algorithm show some agreement with the previous study [6], but also some differences. For example, in 2016, the hydrocarbons detected are evenly distributed, whereas in 2014, they are more dispersed. The difference could be related to temperature, which influences the oxidation and biodegradation of hydrocarbons. Detection is also affected by vegetation, which can generate false alarms, particularly in dry vegetation [25] [27] [28]. The vegetation cover of Madingo-Kayes is dominated by a forest-savannah mosaic, so the savannah can generate a large number of false alarms.

Furthermore, the results obtained with the SAM classification do not agree with those found by [6] [16] [19] [25] [28]. Unlike Madingo-Kayes, where hydrocarbon indices vary in size and are scattered, they are more concentrated along coastlines in other regions such as Louisiana [16] [25] [28] and Liaodong Bay in China [19], where spills are more significant. The same is true in the Djéno terminal area [6], which handles approximately 95% of Congo's crude oil production, or approximately 252,000 bbl/d. The difference with Madingo-Kayes could be explained by the smaller quantity of hydrocarbons spilled in this area. Petroleum hydrocarbons escape easily during extraction, transport, and refining and harm the sustainable development of the environment when they penetrate the soil [18].

The results obtained are similar to those based solely on the calculation of the HI ratio, with slightly fewer false alarms on inland vegetation. However, the classification method gives better results than those obtained with the HI ratio calculation method, as some contaminated coastlines not detected by the latter method are mapped with the classification based on spectral signatures [25] [28].

The results obtained with SSM classification show agreement with those obtained by [6], in that they are very similar to those of SAM classification and the HD ratio.

Given that in the field, [6] found that the distribution of vegetation stress was consistent with that of the indices obtained by SSM classification and that this was linked to the presence of hydrocarbons in this area, probably methane burned and released into the air by the Djéno flare, we believe that the appropriate methodological approach would make it possible to highlight the contamination of vegetation by hydrocarbons in the Madingo-Kayes sector. [30]-[32] demonstrated that vegetation could be used as an indicator of soil contaminated by hydrocarbons. Laboratory analyses of sediments have revealed the presence of hydrocarbons along the Congolese coast, particularly in the Emeraude field area [9]. Given that in our context, vegetation stress evolves in line with the attenuation of hydrocarbon pollution, we believe that the field results, combined with the physico-chemical and biological analyses of the soil on the one hand, and the biophysical and biochemical analyses of the vegetation on the other, would validate the results we obtained using the SSM classification.

The classification methods (SAM and SSM) yielded more satisfactory results than those obtained from the calculation of sub-band ratios (HD and HI), which produce numerous false alarms. The confusion matrices of the different classification methods provided an overall accuracy of 100% and a Kappa coefficient of 1. This overall accuracy is close to that obtained by [14] in the southern part of the border region of Dera Ismail Khan (Pakistan), which ranged between 75 and 100%. The locations identified by the seepage spectra were confirmed in the field and proved to be correct. While the hybrid classification based on CHI-SAM revealed detailed information on spills in the Bohai Sea with an overall accuracy of 84% [19], which is 16% less than the overall accuracy obtained on the Madingo-Kayes images. Unlike [28], we believe that of the two methods used, only classification based on spectral signatures (endmembers) can better detect oil spills on coastlines with very few false alarms, even in the presence of dry vegetation, and does not require field or laboratory measurements. Calculating indices, on the other hand, requires knowledge of the elements in advance in order to reduce the false alarm rate.

6. Conclusions

This study focused on analyzing coastal pollution caused by hydrocarbons in the Madingo-Kayes area using hyperspectral images. The main objective was to detect and map the presence of hydrocarbons on the surface in order to better understand their dynamics over time and space. To this end, several methods were used, including the calculation of sub-band ratios (HD and HI) and classification methods (SAM and SSM).

The results obtained show a notable change between 2014 and 2016. In 2014, the HD ratio identified 443 hydrocarbon indices, distributed between two wavelength ranges: 1700 - 1800 nm (167 indices) and 2300 - 2350 nm (276 indices). In 2016, this number increased to 629 indices, with 177 in the first range and 452 in the second. The HI method also detected a decrease in 2016 compared to 2014, from

155 to 133 indices, but with a different distribution across wavelength ranges. The SAM classification revealed a sharp decrease in the number of hydrocarbon indices, from 387 in 2014 to only 73 in 2016, indicating a significant improvement in environmental quality in this area. Finally, the SSM classification, focusing on vegetation in the 680 - 740 nm range, detected 168 indices in 2014 compared to 18 in 2016, highlighting a reduction in vegetation pollution linked to hydrocarbons.

These results suggest a significant improvement in the environmental situation between 2014 and 2016. Oil pollution appears to have decreased, which could be explained by changes in human activities, oceanographic conditions, and climate. The ability of classification methods to provide reliable data shows that hyperspectral imaging is a valuable tool for remote monitoring of coastal pollution. It allows the extent and dynamics of contamination to be assessed, both on land and at sea.

However, to reinforce the validity of these results, it is essential to supplement this study with in situ measurements and laboratory analyses. These samples will enable the calibration and validation of the hydrocarbon indices detected by imaging, thus ensuring greater accuracy in the assessment of pollution.

Looking ahead, we hope that studies will be multiplied to extend the field of observation of hydrocarbon pollution using hyperspectral imaging. To this end, we propose studies on the influence of temperature on hydrocarbons and the estimation of the quantity evaporated into the atmosphere, the assessment of the physico-chemical and biological quality of water and soil exposed to hydrocarbons, the estimation of the quantity of hydrocarbons infiltrated into the soil, biophysical and biochemical analysis of vegetation exposed to hydrocarbons, assessment of the degree of hydrocarbon pollution on pelagic and benthic microfauna and on benthic macrofauna, and assessment of the degree of hydrocarbon pollution on socio-economic activities.

Looking ahead, we would like to see more studies conducted to expand the scope of observation of oil pollution using hyperspectral imaging. To this end, we propose studies on the influence of temperature on hydrocarbons and the estimation of the quantity evaporated into the atmosphere, the assessment of the physico-chemical and biological quality of water and soil exposed to hydrocarbons, the estimation of the quantity of hydrocarbons infiltrated into the soil, biophysical and biochemical analysis of vegetation exposed to hydrocarbons, assessment of the degree of pollution caused by hydrocarbons on pelagic and benthic microfauna and on benthic macrofauna, and assessment of the degree of pollution caused by hydrocarbons on socio-economic activities.

Given the vulnerability of the Congolese coastline to frequent oil spills, it is crucial to implement sustainable management measures to mitigate these impacts. Proposed strategies include the use of oil booms, pumps, mechanical or manual skimmers, and absorbents to clean up contaminated areas. Other techniques, such as sediment washing, submerged mixing, sand screening, biostimulation, bioaugmentation, and natural wave cleaning, are also recommended to limit the spread of pollution and protect coastal ecosystems and human health.

Conflicts of Interest

The authors declare no conflicts of interest regarding the publication of this paper.

References

[1] EITI CONGO (2018) Extractive Industries Transparency Initiative. Report.

[2] APEGG (2006) Assessment of the Burden of Environmental Diseases on the Congolese Coast (Pointe-Noire, Congo). Study Report. https://www.cesbc.org/developpement_durable/environnement/kouilou/textes/rapport_evaluation_maladie.pdf

[3] World Bank (2012) Republic of Congo, Mining Sector Review. Mining, Oil and Gas Department.

[4] CPIB (2009) Emergency Response Plan for Oil Pollution (PNUI), Revised 2009. Updated in Accordance with the Recommendations of the 2006, 2007 and 2009 Workshops. Ministry of Transport, Civil Aviation and Merchant Shipping, Deputy Minister for Merchant Shipping.

[5] APEGG (2005) Environmental Assessment of Oil Pollution on the Kouilou Coast (Congo). Study Report. https://www.cesbc.org/developpement_durable/environnement/kouilou/textes/rapport_d_expertise_allemande.pdf

[6] Bawatokobuta Nanitelamio, A.M. (2020) Contribution of Remote Sensing to the Analysis of the Potential Effects of Hydrocarbon Exploitation along the Congolese Coast: Use of Hyperion EO-1 Hyperspectral Images. Master's Thesis, Marien Ngouabi University.

[7] Konan, K.E. and Nziengui, H.S.J. (2022) Remote Sensing Assessment of Marine Oil Pollution in Gabon from 2015 to 2017: The Case of Port-Gentil and Mayumba. *Revue de l'environnement et de la biodiversité*, **7**, 1-20.

[8] Najoui, Z., Amoussou, N., Riazanoff, S., Aurel, G. and Frappart, F. (2022) Oil Slicks in the Gulf of Guinea—10 Years of Envisat Advanced Synthetic Aperture Radar Observations. *Earth System Science Data*, **14**, 4569-4588. https://doi.org/10.5194/essd-14-4569-2022

[9] Edou, M. (2002) Impact of Oil Exploitation on the Environment: The Case of the Emeraude Field in Congo Brazzaville. *Geo-Eco-Top*, **26**, 57-72.

[10] Pabou Mbaki, E. (2003) The Congo Defenseless against Oil Pollution. Vertigo, Regards/Terrain. https://doi.org/10.4000/vertigo.4856

[11] RPDH and CJP (2009) Oil Exploitation and Human Rights in Congo Brazzaville. Report, 5p+Annexes.

[12] ITOPF (2013) Effects of Oil Pollution on the Environment. Technical Information Guide. https://itopf.org/knowledge-resources/documents-guides/tip-13-effects-of-oil-pollution-on-the-marine-environment/

[13] Kimbatsa, F.G., Boungou, G. and Ngouma, D. (2016) Artisanal Fishing in Madingo-Kayes: Between Subsistence and Commercial Endeavours. Caribbean Studies. https://doi.org/10.4000/etudescaribeennes.10391

[14] Khan, S., Rahman, S., Haq, M. and Munir, S. (2016) Hyperspectral Remote Sensing for the Detection of Natural Hydrocarbon Seeps. *Asian Journal of Multidisciplinary Studies*, **4**, 1-10.

[15] Smejkalová, E., Bujok, P. and Pikl, M. (2017) Study of Old Ecological Hazards, Oil

Seeps and Contaminations Using Earth Observation Methods—Spectral Library for Oil Seep. *Archives of Environmental Protection*, **43**, 3-10. https://doi.org/10.1515/aep-2017-0001

[16] Khanna, S., Santos, M.J., Ustin, S.L., Shapiro, K., Haverkamp, P.J. & Et Lay, M. (2018) Comparing the Potential of Multispectral and Hyperspectral for Monitoring Oil Spill Impact. *Sensors*,**18**, Article No. 558 https://doi.org/10.3390/s18020558

[17] Ranarison, F.J.M.V. (2019) Detection of Surface Hydrocarbon Indices from Hyperion Data: Case of Block 3102 in the Southern Sector of Bemolanga. Master II Thesis in Geological Engineering, University of Antananarivo.

[18] Chen, C., Jiang, Q., Zhang, Z., Shi, P., Xu, Y., Liu, B., *et al*. (2020) Hyperspectral Inversion of Petroleum Hydrocarbon Contents in Soil Based on Continuum Removal and Wavelet Packet Decomposition. *Sustainability*, **12**, Article 4218. https://doi.org/10.3390/su12104218

[19] Deepthi and Thomas, T. (2020) Spectral Similarity Algorithm-Based Image Classification for Oil Spill Mapping of Hyperspectral Datasets. *Journal of Spectral Imaging*, **9**, a14.

[20] Hörig, B., Kühn, F., Oschütz, F. and Lehmann, F. (2001) Hymap Hyperspectral Remote Sensing to Detect Hydrocarbons. *International Journal of Remote Sensing*, **22**, 1413-1422. https://doi.org/10.1080/01431160120909

[21] Qingjiu, T., Yi, L. and Lei, Z. (1992) A Remote Sensing Basic Study on the Relation between Spectral Properties (0.40-1.10 μm) of the Oil and Gas Microseepage in East Hebei Province. *Proceedings of the Asian Conference on Remote Sensing*, Mongolia, 7 October 1992.

[22] Cloutis, E.A. (1989) Spectral Reflectance Properties of Hydrocarbons: Remote-Sensing Implications. *Science*, **245**, 165-168. https://doi.org/10.1126/science.245.4914.165

[23] Kühn, F. and Hörig, B. (1996) Environmental Remote Sensing of Military Exercise Areas in Germany. In: *Remote Sensing and GIS for Site Characterization*: *Applications and Standards*, ASTM International, 107-116. https://doi.org/10.1520/stp18259s

[24] Ellis, J.M., Davis, H.H. and Quinn, M.B. (2000) Airborne Hyperspectral Imagery for the Petroleum Industry. *Proceedings of the* 14*th International Conference on Applied Geologic Remote Sensing*, Las Vegas, 6-8 November 2000, 89-96.

[25] Achard, V., Foucher, P.Y. and Dubucq, D. (2021) Hydrocarbon Pollution Detection and Mapping Based on the Combination of Various Hyperspectral Imaging Processing Tools. *Remote Sensing*, **13**, Article 1020. https://doi.org/10.3390/rs13051020

[26] Short, N. (1998). Finding Oil and Gas in Oklahoma, the Remote Sensing Tutorial (An Online Handbook). Code 935, Goddard Space Flight Center, NASA. http://priede.bf.lu.lv/GIS/.Descriptions/RST/Sect5/nicktutor_5-4.shtml

[27] Kühn, F., Oppermann, K. and Hörig, B. (2004) Hydrocarbon Index—An Algorithm for Hyperspectral Detection of Hydrocarbons. *International Journal of Remote Sensing*, **25**, 2467-2473. https://doi.org/10.1080/01431160310001642287

[28] Achard, V. and Elin, C. (2019) Automatic Mapping of Hydrocarbon Pollution Based on Hyperspectral Imaging. 2019 *IEEE International Geoscience and Remote Sensing Symposium*, Yokohama, 28 July-2 August 2019, 5678-5771. https://doi.org/10.1109/igarss.2019.8898455

[29] Noomen, M.F., van der Werff, H.M.A. and van der Meer, F.D. (2012) Spectral and Spatial Indicators of Botanical Changes Caused by Long-Term Hydrocarbon Seepage.

Ecological Informatics, **8**, 55-64. https://doi.org/10.1016/j.ecoinf.2012.01.001

[30] Arellano, P., Tansey, K., Balzter, H. and Boyd, D.S. (2015) Detecting the Effects of Hydrocarbon Pollution in the Amazon Forest Using Hyperspectral Satellite Images. *Environmental Pollution*, **205**, 225-239. https://doi.org/10.1016/j.envpol.2015.05.041

[31] Lassalle, G., Credoz, A., Hédacq, R., Fabre, S., Dubucq, D. and Elger, A. (2018) Assessing Soil Contamination Due to Oil and Gas Production Using Vegetation Hyperspectral Reflectance. *Environmental Science & Technology*, **52**, 1756-1764. https://doi.org/10.1021/acs.est.7b04618

[32] Vennetier, P. (1966) Geography of Congo-Brazzaville, Higher Education in Central Africa. Gautier-Villars-Paris.

[33] Samba-Kimbata, M.J. (1978) Climate of the Lower Congo. Doctoral Thesis, University of Burgundy.

[34] Vennetier, P. (1968) Pointe-Noire and the Coastline of Congo-Brazzaville.

[35] Descoings, B. (1975) The Major Natural Regions of Congo. *Candollea*, **30**, 91-120.

[36] Kimpouni, V., Loumeto, J.J. and Mizingou, J. (2008) Floristic Diversity of the *Aucoumea klaineana* (Okoumé) Forest Facies on the Congolese Coast. *Acta Botanica Gallica*, **155**, 323-334. https://doi.org/10.1080/12538078.2008.10516113

[37] Miabangana, E.S., Nsongola, G., Orban, B., Van Rooyen, M., Van Rooyen, N. and Gaugris, J. (2017) Floristic and Phytogeographic Analysis of Coastal and Sub-Coastal Vegetation in Kouilou (Republic of Congo). *International Journal of Innovation and Applied Studies*, **19**, 206-217.

[38] Bocquier, G. and Guillemin, R. (1959) Overview of the Main Soil Formations in the Republic of Congo. ORSTOM.

[39] Jamet, R. and Rieffel, J.M. (1976) Soil Map of Congo at 1/200,000, Pointe-Noire Sheet, Loubomo Sheet. Explanatory Note No. 65. ORSTOM.

[40] Callec, Y., Lasseur, E., Le Bayon, B., Thieblemont Fullgraf, T., Gouin, J., *et al*. (2015) Explanatory Note for the Pointe-Noire Sheet at 1:200,000. National Geological Mapping Programme. Ministry of Mines and Geology. Directorate General of Mines and Geology. BRGM Publications.

[41] Roques, J.M. (2013) Hydro-Sedimentary Study of the Relocation Site for Fishermen in Pointe-Noire Bay. Final Report Version V1.0, AMENIS.

[42] Giresse, P. (1980) Sedimentological Map of the Congo Continental Shelf, Explanatory Note No. 85. ORSTOM.

[43] Samba, G. (2020) The Climate of Congo-Brazzaville. Preface by Professor Dominique Nganga. L'Harmattan.

[44] EROS (2020) Earth Observing 1 (EO-1). https://eo1.gsfc.nasa.gov/

[45] USGS (2013) Earth Observing-1 (EO-1) Hyperion. https://earthexplorer.usgs.gov/

[46] EITI CONGO (2014) Extractive Industries Transparency Initiative. Report, 94.

[47] EITI CONGO (2016) Extractive Industries Transparency Initiative. Report, 159.